# Novel method to operation conditions identification of high-order power converters ☆

Guidong Zhang [a,*], Haodong Chen [a], Samson Shenglong Yu [b], Zhong Li [c]

[a] Guangdong University of Technology, Guangzhou 510006, PR China
[b] Deakin University, Victoria, Australia
[c] FernUniversität in Hagen, 58084 Hagen, Germany

## HIGHLIGHTS

- Derivation of HOPCs modes via a proposed approach to identify boundary conditions.
- A 3-Z-network converter is demonstrated as a typical study.
- With the proposed method, unexpected operation modes can be avoided.
- Simulations are presented to well verify the proposed method.
- A prototype is conducted to validate the effectiveness of the proposed approach.

## GRAPHICAL ABSTRACT
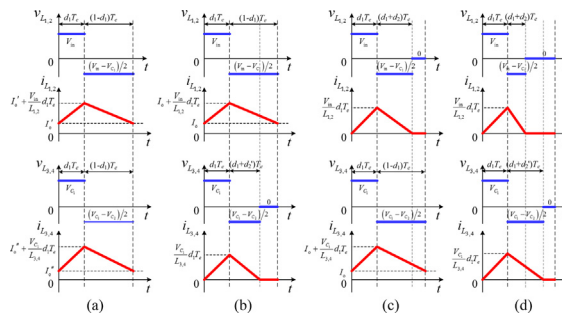
## ABSTRACT

Introduction: Intermittent solar energy causes different operational modes of power converters including continuous current modes (CCMs) and discontinuous current modes (DCMs), which need appropriate control strategies and parameters assignment to ensure the functionality of the overall solar energy power generation system. Hence, it is important to identify suitable operation modes for a high-order converter system. However, for a high-order power converter (HOPC), traditional time-domain analysis method and bifurcation analysis are inapplicable, since this requires comprehensive analysis and sophisticated control design.

Objectives: To improve reliability and reduce mathematical complexity, this paper focuses on the operation mode derivation of HOPCs to well identify its boundary conditions and provide industry standards for converter applications.

Methods: With complex operation modes, 3-Z-network converter is analysed as a typical example and its derivations of boundary conditions are elaborated. In detail, the equilibrium points and boundary conditions of each operation modes are first derived; then with the guidance of boundary conditions, unexpected operation modes can be avoided by parameters reassignment.

Results: Simulations and experimentation on the newly established system prototype are conducted to validate the effectiveness of the proposed approach. It demonstrates that the theoretical and experimental boundary conditions are in good agreement.

Conclusion: This paper provides equilibrium points and boundary conditions, and obtains deeper insights into the behaviors of the 3-Z-network converter. The derivations of four operation modes and the boundary condition of each mode has been conducted and provided for the large-signal averaged model of the converter, which provides guidance for engineers to adjust the system parameters so as to realize

required operation modes. Simulation and experimentation have verified the accuracy and effectiveness of the proposed identified operation boundaries.

## Introduction

In the past decades, the renewable energy sector has received substantial investment in infrastructural development. However, for renewable energy integrated energy systems, the technical requirements for power electronics devices have been raised significantly. Firstly, high-ratio boosting techniques with high efficiency and reliability are required to boost low DC voltage generated by renewable energy for grid connection [1–3]. Secondly, effective and efficient modeling and control techniques are needed to compensate for renewable source's intermittency and uncertainty features to realize the system's best working condition [4,5].

With the advantages of simple structure, high efficiency and high reliability, single-stage high-step-up converters are one of the main methods to realize high voltage conversion ratio [1,6]. A large quantity of single-stage high-step-up converters combining switched-inductors, switched-capacitors, impedance networks, magnetic coupling devices have been proposed [6–11]. However, few high-step-up converters manage to address and overcome the problems associated with intermittent renewable energy sources, with a majority of them focused on continuous current modes (CCMs) only. With the variation of load, switching frequency and intermittent input voltage, the currents flowing through inductors may reduce to zero and the high-step-up converters will then operate in discontinuous conduction modes (DCMs) [12]. This leads to high input current distortion because of a low gain in CCMs controller, which is inapplicable for DCMs [13,14]. Moreover, different operation modes produce distinct devices stresses, leading to inapplicability between CCMs and DCMs, electromagnetic interference (EMI) increase and power loss [14–16], which further lead to damage of converters. For better converter design, the boundary conditions of CCMs and DCMs should be well distinguished for power converters connected to renewable sources.

It is noted that power converters are nonlinear systems which are susceptible to factors that may lead to instability [17–20]. A small change of parameters can lead to bifurcation and deviation from the predefined equilibrium point [21–23]. To find out the operation boundaries of a converter, frequency domain analysis methods can be utilized. However, it requires a large amount of computation [24]. Therefore, another traditional method, i.e., time-domain analysis method based on the average model, has been widely used [25–27]. Furthermore, based on the time-domain analysis method, many modelling methods are proposed, such as circuit averaging and state-space modeling [28–30]. However, it is difficult to build mathematical models for HOPCs. To deal with this issue, a harmonic analysis method was proposed to identify the criteria of different loading conditions to operate at DCMs [31]. However, it bears great inaccuracies and the stability near the switching frequency is unpredicted by time-domain methods. [21]. Compared to time-domain analysis method, boundary conditions for system parameters can be deduced through bifurcation analysis. However, involved mathematical derivations are required and it is difficult to build accurate models [21].

To improve reliability and reduce mathematical complexity, this paper focuses on the operation mode derivation of HOPCs to well identify its boundary conditions and provide industry standards for converter applications. With complex operation modes, 3-Z-network converter proposed in [32] is analysed as a typical example and its derivations of boundary conditions are elaborated.

The remainder of this paper is organized as follows. Section 'An example: Equilibrium points identification for 3-Z-network converter' presents four operation modes of 3-Z network converter and gives the equilibrium point of each mode. Based on the derived points, the boundary condition of each mode is illustrated in Section 'Boundary conditions identification'. Then, simulation and experimentation are conducted in Sections 'Simulation' and 'Experimentation' to verify the proposed analytical approach for boundary identification. Finally, a conclusion is given in Section 'Conclusion'.

## An example: Equilibrium points identification for 3-Z-network converter

Combined with two switched-inductors, a 3-Z-network converter proposed in [32] is taken as an example in this study and its schematic is shown in Fig. 1.

Denote $< \cdot >_{T_e}$ as the average value during period $[0, T_e]$, where $T_e$ is the switching period. In order to make it easier to understand, $d_1 T_e$ is the period that switch is on; $d_2$ and $d_2'$ are duty cycles of the two boost stages in DCM, respectively. To simplify the analysis without loss of generality, we impose the following assumptions:
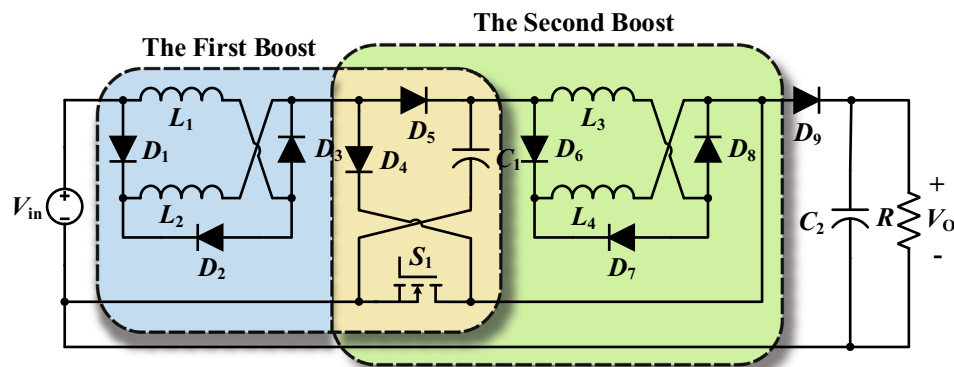


**Fig. 1.** Schematic of the 3-Z-networks boot converter.
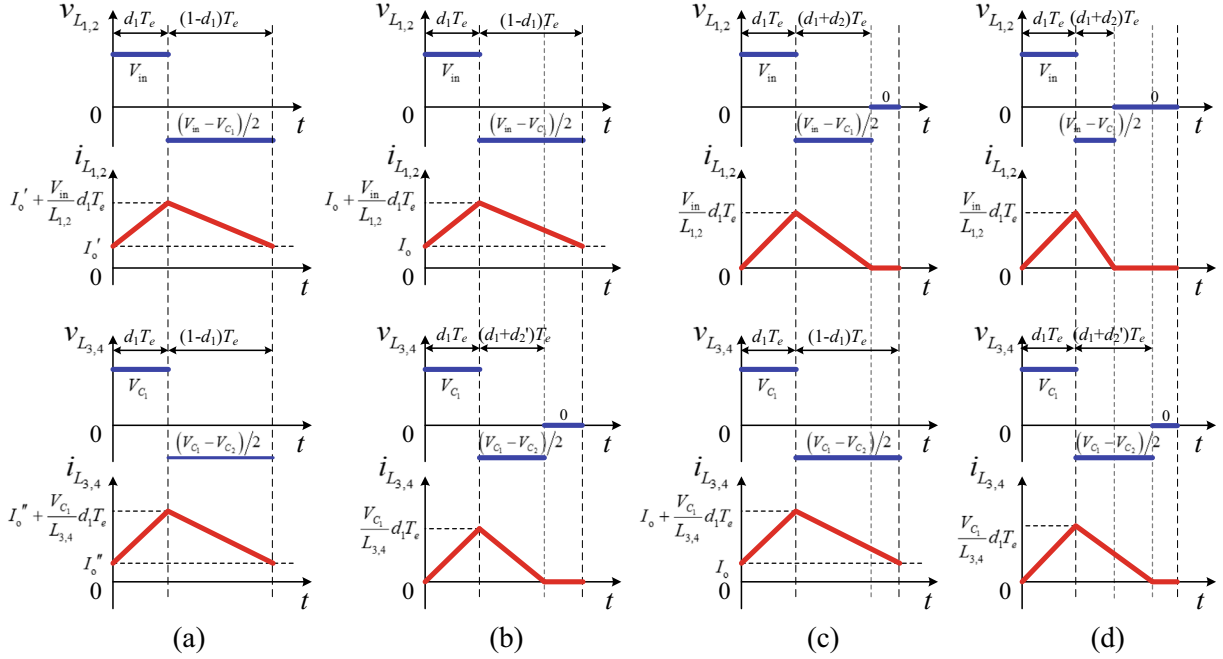
**Fig. 2.** The voltage and current waveforms of $L_1, L_2, L_3$ and $L_4$ in each operation mode. (**a**) Case I: $C - C$; (**b**) Case II: $C - D$; (**c**) Case III: $D - C$; (**d**) Case: IV $D - D$.

1) All the components are ideal;
2) Filter capacitors $C_1$ and $C_2$ are large enough that the voltages across them are constant.
3) $L_1 = L_2 = L_{1,2}$ and $L_3 = L_4 = L_{3,4}$, hence, $i_{L_1} = i_{L_2} = i_{L_{1,2}}$, $i_{L_3} = i_{L_4} = i_{L_{3,4}}$, $v_{L_1} = v_{L_2} = v_{L_{1,2}}$ and $v_{L_3} = v_{L_4} = v_{L_{3,4}}$.

According to the inductor current in each boost stage, four operation modes are briefed as follows, and the waveforms of voltage and current across four inductors are shown in Fig. 2. Case I represents that all currents across four inductors are continuous, represented as $C - C$; Case II is that $i_{L_1}$ and $i_{L_2}$ reduce to zero, but $i_{L_3}$ and $i_{L_4}$ are continuous ($C - D$), while Case III is the opposite case of Case II ($D - C$); and Case IV represents that $i_{L_1}, i_{L_2}, i_{L_3}$ and $i_{L_4}$ are all discontinuous ($D - D$).

Due to the two uncertain duty ratios $d_2$ and $d_2'$, Case IV ($D - D$) is the most complicated and its derivation will be deduced as a typical example. As shown in Fig. 2 (d), $(d_1 + d_2)T_e$ is the instant that the currents across inductors $L_1$ and $L_2$ reduce to zero. Moreover, inductors $L_3$ and $L_4$ are cut off in the interval $[(d_1 + d_2')T_e, T_e]$.

The average currents through inductors $L_1, L_2, L_3$ and $L_4$ can be deduced as

$$I_{L_{1,2}} = \frac{V_{in}}{2L_{1,2}} d_1 T_e, \tag{1}$$

and

$$I_{L_{3,4}} = \frac{V_{C_1}}{2L_{3,4}} d_1 T_e. \tag{2}$$

In terms of the voltage-second constant theory, we have

$$< v_{L_{1,2}} >_{T_e} = d_1 < v_{in} >_{T_e} + d_2 \frac{< v_{in} >_{T_e} - < v_{C_1} >_{T_e}}{2} = 0. \tag{3}$$

Ignoring the impact of ac small signals at the steady state, we have

$$M_1 = \frac{V_{C_1}}{V_{in}} = \frac{2d_1 + d_2}{d_2}. \tag{4}$$

Similarly, we can obtain the ratio of $V_{C_1}$ and $V_{C_2}$ as

$$M_2 = \frac{V_{C_2}}{V_{C_1}} = \frac{2d_1 + d_2'}{d_2'}, \tag{5}$$

where $M_1$ and $M_2$ denote the voltage gains of the first and second boost stages in Fig. 1, respectively, and hence, the voltage gain $M$ of the converter is equal to $M_1 \cdot M_2$.

Based on energy conservation, the energy released from $L_3$ and $L_4$ during the interval $[d_1 T_e, (d_1 + d_2')T_e]$ is equal to the energy dissipation through the load $R$ in a switching period $T_e$. Hence, one can obtain a quadratic equation as

$$\frac{V_{C_1}}{2L_{3,4}} d_1 T_e V_{C_2} d_2' T_e = \frac{V_{C_2}^2}{R} T_e, \tag{6}$$

i.e.,

$$d_2' = \frac{K_2(1 + \sqrt{1 + 4d_1^2/K_2})}{d_1}, \tag{7}$$

where $K_2 = L_{3,4}/(RT_e)$. Similarly, we can have

$$\frac{V_{in}}{2L_{1,2}} d_1 T_e V_{C_1} d_2 T_e = \frac{V_{C_2}^2}{R} T_e, \tag{8}$$

which is solved as

$$d_2 = \frac{K_1}{d_1}\left(\frac{2d_1 + d_2'}{d_2'}\right)^2 + \sqrt{\frac{K_1^2}{d_1^2}\left(\frac{2d_1 + d_2'}{d_2'}\right)^4 + 4K_1\left(\frac{2d_1 + d_2'}{d_2'}\right)^2}, \tag{9}$$

where $K_1 = L_{1,2}/(RT_e)$. Therefore, the duties $d_2$ and $d_2'$, gains $M_1$ and $M_2$, and currents are denoted as the functions of $d_1$, which are listed in Table 1. Similarly with the derivation above, the equilibrium points of Cases I~III are also listed in Table 1.

**Table 1**
Equilibrium points of each mode.

| Parameter | Case I | Case II | Case III | Case IV |
|---|---|---|---|---|
| $d_2$ | | | $\frac{K_1}{d_1}M_2^2 + \sqrt{\frac{K_1^2}{d_1^2}M_2^4 + 4K_1 M_2^2}$ | $\frac{K_1}{d_1}M_2^2 + \sqrt{\frac{K_1^2}{d_1^2}M_2^4 + 4K_1 M_2^2}$ |
| $d\prime_2$ | | $\frac{K_2}{d_1} + \sqrt{\frac{K_2^2}{d_1^2} + 4K_2}$ | | $\frac{K_2}{d_1} + \sqrt{\frac{K_2^2}{d_1^2} + 4K_2}$ |
| $M_1$ | $\frac{1+d_1}{1-d_1}$ | $\frac{1+d_1}{1-d_1}$ | $\frac{1}{2} + \frac{1}{2}\sqrt{1 + \frac{4d_1^2}{K_1} \cdot M_2^{-2}}$ | $1 + 2\frac{d_1}{d_2}$ |
| $M_2$ | $\frac{1+d_1}{1-d_1}$ | $\frac{1}{2} + \frac{1}{2}\sqrt{1 + \frac{4d_1^2}{K_2}}$ | $\frac{1+d_1}{1-d_1}$ | $1 + 2\frac{d_1}{d\prime_2}$ |
| $I_{L_{1,2}}$ | $\frac{V_{in}(1+d_1)^3}{R(1-d_1)^4}$ | $\frac{2d_1+d_2\prime}{1-d_1}I_{L_{3,4}}$ | $\frac{V_{in}d_1 T_e}{2L_{1,2}}$ | $\frac{V_{in}d_1 T_e}{2L_{1,2}}$ |
| $I_{L_{3,4}}$ | $\frac{V_{in}(1+d_1)^2}{R(1-d_1)^3}$ | $\frac{M_1 V_{in}d_1 T_e}{2L_{3,4}}$ | $\frac{d_2}{1+d_1}I_{L_{1,2}}$ | $\frac{M_1 V_{in}d_1 T_e}{2L_{3,4}}$ |

**Table 2**
Boundary conditions of each operating mode.

| Operating mode | Boundary Conditions |
|---|---|
| Case I | $K_{1\_C-C}^{crit}(d_1) = \frac{(1+d_1)^3}{(1-d_1)^4 d_1} > \frac{1}{2K_1}$ |
| | $K_{2\_C-C}^{crit}(d_1) = \frac{1+d_1}{(1-d_1)^2 d_1} > \frac{1}{2K_2}$ |
| Case II | $K_{C-D}^{crit}(d_1) = \frac{(2d_1+d_2\prime)(1+d_1)}{(1-d_1)^2} > \frac{L_{3,4}}{L_{1,2}}$ |
| | $d_1 + d_2\prime < 1$ |
| Case III | $K_{D-C}^{crit}(d_1) = \frac{d_2}{(1+d_1)M_1} > \frac{L_{1,2}}{L_{3,4}}$ |
| | $d_1 + d_2 < 1$ |
| Case IV | $d_1 + d_2 < 1$ |
| | $d_1 + d\prime_2 < 1$ |

**Table 3**
Parameters of the converter in the simulation.

| Parameter | Value | | |
|---|---|---|---|
| | Set I | Set II | Set III |
| Input voltage ($V_{in}$) | 10 V | 2 V | 2 V |
| Switching period ($T_e$) | 100 μs | 100 μs | 100 μs |
| Capacitor ($C_1$) | 1000 μF | 1000 μF | 1000 μF |
| Capacitor ($C_2$) | 500 μF | 500 μF | 500 μF |
| Inductance ($L_1, L_2$) | 0.2 mH | 0.2 mH | 0.2 mH |
| Inductance ($L_3, L_4$) | 0.7 mH | 0.2 mH | 0.2 mH |
| Load ($R$) | 80–600Ω | 20Ω | 100Ω |
| Duty ($d_1$) | 0.1–0.6 | 0.7 | 0.35 |

## Boundary conditions identification

As shown in Fig. 2 (a), the converter is working in Case I ($C - C$) if and only if $I'_o > 0$ and $I''_o > 0$ according to the definitions of CCM and DCM. Hence, average currents $I_{L_{1,2}}$ and $I_{L_{3,4}}$ are larger than half of the current ripple values of $i_{L_{1,2}}$ and $i_{L_{3,4}}$, i.e.,

$$I_{L_{1,2}} > \frac{1}{2} \cdot \frac{V_{in}d_1 T_e}{L_{1,2}}, \tag{10}$$

and

$$I_{L_{3,4}} > \frac{1}{2} \cdot \frac{V_{C_1}d_1 T_e}{L_{3,4}}. \tag{11}$$

Substituting $I_{L_{1,2}}$ of Case I in Table 1 into the equations above leads to the existence boundary condition of Case I, as follows,

$$K_{1\_C-C}^{crit}(d_1) = \frac{(1+d_1)^3}{(1-d_1)^4 d_1} > \frac{1}{2} \cdot \frac{RT_e}{L_{1,2}} = \frac{1}{2K_1}, \tag{12}$$

and

$$K_{2\_C-C}^{crit}(d_1) = \frac{1+d_1}{(1-d_1)^2 d_1} > \frac{1}{2K_2}, \tag{13}$$

where $K_{1\_C-C}^{crit}(d_1)$ and $K_{2\_C-C}^{crit}(d_1)$ are two functions of $d_1$ corresponding to the first and second boost stages in Case I. Similarly, we can obtain boundary conditions of each operation mode as Table 2.

A numerical example is provided to illustrate the process of mode identification. We assign $R = 180\Omega, T_e = 100$ μs, $L_{1,2} = 0.2$ mH, $L_{3,4} = 0.7$ mH, $V_{in} = 10$ V and $d_1 = 0.2$, thus



**Fig. 3.** Boundary conditions with varying of $L_{3,4}$ when $T_e = 100$ μs, $L_{1,2} = 0.2$ mH, $V_{in} = 10$ V. (a) $L_{3,4} = 0.7$ mH; (b) $L_{3,4} = 0.5$ mH; (c) $L_{3,4} = 0.3$ mH.
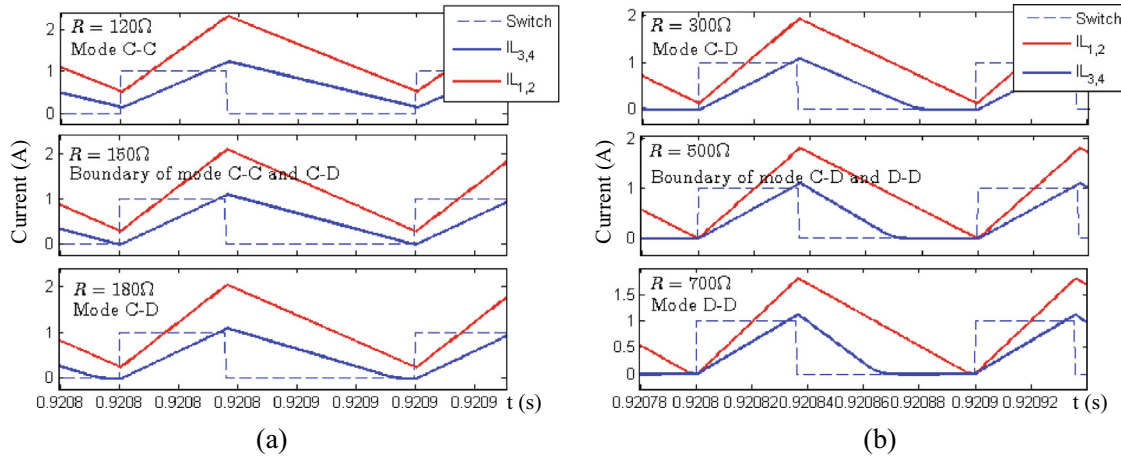
**Fig. 4.** Boundary conditions and current waveforms when $d_1 = 0.36$. (**a**) Boundary condition $d_1 = 0.36$ and $R = 150\Omega$ between $C - C$ and $C - D$; (**b**) Boundary condition $d_1 = 0.36$ and $R = 500\Omega$ between $C - D$ and $D - D$.
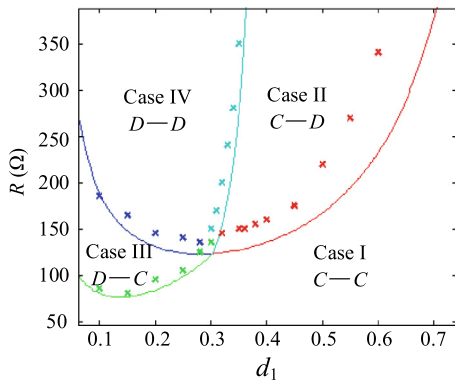


**Fig. 5.** Boundary conditions for $d_1$ and $R$ in theory and simulation.

$1/(2K_1) = 45$ and $1/(2K_2) = 12.86$. With Table 1, we can obtain that $K_{1\_C-C}^{crit}(d_1) = 21.09$ and $K_{2\_C-C}^{crit}(d_1) = 9.38$ for Case I; $d_1 + d_2' = 0.83$ and $K_{C-D}^{crit}(d_1) = 1.94$ for Case II; $d_1 + d_2 = 0.67$ and $K_{D-C}^{crit}(d_1) = 0.21$ for Case III; and $d_1 + d_2 = 0.72$ and $d_1 + d_2' = 0.83$ for Case IV. In terms of Table 2, only the condition $d_1 + d_2 < 1, d_1 + d_2' < 1$ of Case IV is valid. Hence, the mode of the converter is determined as Case IV as shown the point $A$ in Fig. 3(a).

Parameters $d_1$ and $R$ vary in practical applications, such as PV systems. In consequence, the operation modes of the converter can be modelled as functions of these two variables. Under the guidance of Table 2, the boundary condition of each mode can be depicted as two or four curves in Fig. 3 when $L_{3,4}$ equals 0.7 mH, 0.5 mH and 0.3 mH. Assuming $d_1 = 0.4$ and $R = 70\Omega$ when $L_{3,4} = 0.5$ mH, the converter is in mode Case I as the point $A$ of Fig. 3 (*b*). With the increase of $R$ (from point $A$ to $B$), the mode transfers from Case I to Case II, and the boundary condition is $d_1 = 0.4$ and $R = 97\Omega$. Similarly, with the decrease of $d_1$ (from point $B$ to $C$), the mode transfers from Case II to Case IV, and the boundary condition is $d_1 = 0.27$ and $R = 149\Omega$. In addition, unexpected modes can be avoided by tuning parameters $L_1 \sim L_4$. For instance, Case III is eliminated in Fig. 3 (*c*) with the decrease of $L_{3,4}$.

## Simulation

In this section, MATLAB and Simulink softwares are used to establish the correctness of above mathematical analysis. As listed in Table 3, three sets of component parameters are simulated and obtain validating boundary conditions of Case I and Case II.

Assume the parameters configured as Set I of Table 3, and the current waveforms of $L_{1,2}$ and $L_{3,4}$ are simulated as shown in Fig. 4 when $d_1 = 0.36, R = 120\Omega, R = 150\Omega, R = 180\Omega, R = 300\Omega$, $R = 500\Omega$ and $R = 700\Omega$. The minimum of current $I_{L_{3,4}}$ (the solid blue lines) is greater than zero when $R = 120\Omega$, while current $I_{L_{3,4}}$ is obviously discontinuous when $R = 180\Omega$, and the converter is in the critical condition when $R = 150\Omega$. Hence, one of the boundary conditions between $C - C$ and $C - D$ is $d_1 = 0.36$ and $R = 150\Omega$. Similarly, Fig. 4 (*b*) shows another boundary condition between $C - D$ and $D - D$ when $d_1 = 0.36$ and $R = 500\Omega$. With the increasing of $d_1$ from 0.1 to 0.6, the boundary conditions are measured in the simulation according to the current waveforms of inductors, and the results are plotted in Fig. 5 using cross marks. The simulation results are in good agreement with the theoretical results (solid lines in Fig. 5).

## Experimentation

To verify the correctness of the theoretical analysis, a prototype has been built as shown in Fig. 6. The currents flowing through the four inductors can be measured by the current probe, which indicates the operation modes of CCM or DCM.

According to the derivations mentioned in Section 'Boundary conditions identification', the converter can only operates in Cases I and II with the variation of $R$ and $d_1$ when $L_{1,2} = 2.75$ mH, $L_{3,4} = 0.107$ mH, $C_1 = C_2 = 47$ µF. The theoretical boundary condition in the $d_1 - R$ 2D coordinate plane is depicted with the blue solid line in Fig. 7. In the experiment, the boundary conditions are measured by adjusting the duty cycle $d_1$ when the load $R$ is fixed at 48.4Ω, 50.1Ω, 54.5Ω, 58.9Ω, 61.5Ω, 67.0Ω, 74.2Ω, 82.3Ω, 92.5Ω, 100.0Ω, 154.0Ω, 202.0Ω and 253.0Ω, respectively for each data point. The results are illustrated by red cross marks in Fig. 7. It demonstrates that the theoretical and experimental boundary conditions are in good agreement.

## Conclusion

This paper provides equilibrium points and boundary conditions, and obtains deeper insights into the behaviors of the 3-Z-network converter. The derivations of four operation modes and the boundary condition of each mode has been conducted and pro-
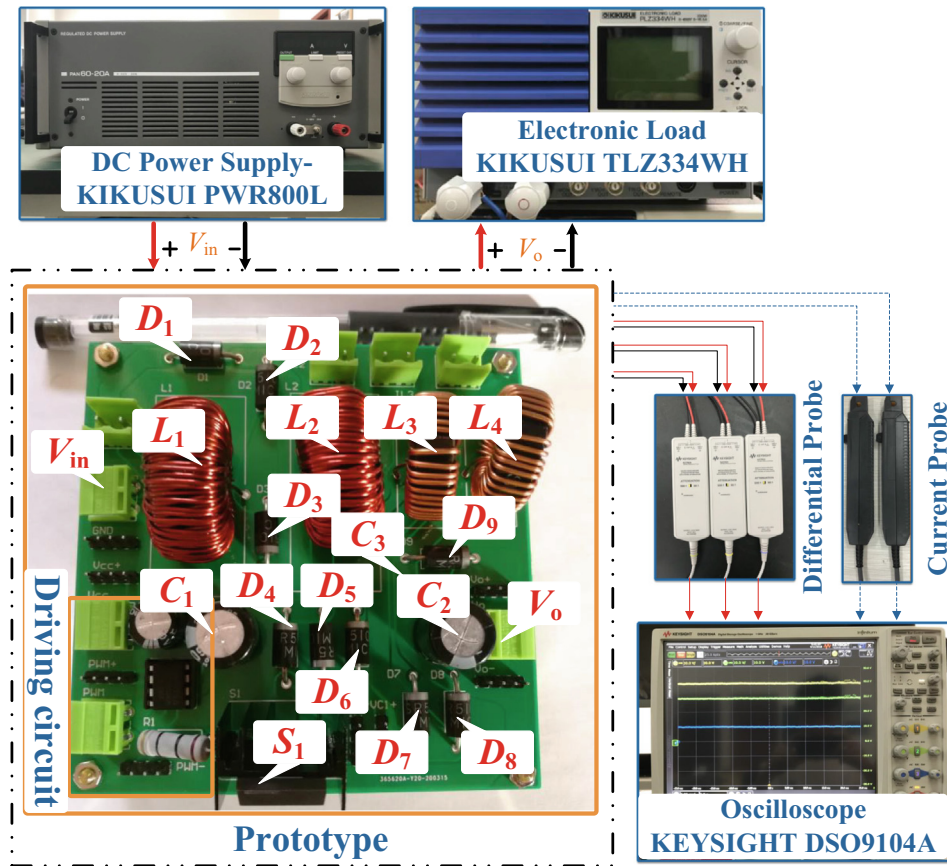
**Fig. 6.** Converter prototype.
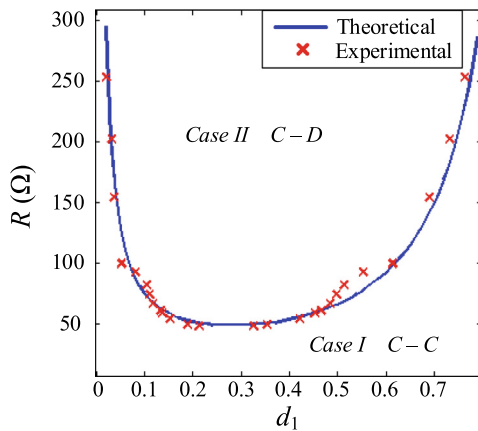


**Fig. 7.** Boundary conditions for $d_1$ and $R$ in theory and experiments.

vided for the large-signal averaged model of the converter, which provides guidance for engineers to adjust the system parameters so as to realize required operation modes. Simulation and experimentation have verified the accuracy and effectiveness of the proposed identified operation boundaries.

## Compliance with Ethics Requirements

This article does not contain any studies with human or animal subjects.

## Declaration of Competing Interest

The authors declare that they have no known competing financial interests or personal relationships that could have appeared to influence the work reported in this paper.

## References

[1] Zhang G, Li Z, Zhang B, Halang WA. Power electronics converters: Past, present and future. Renew Sustain Energy Rev 2018;81:2028–44.

[2] Jupin S, Vechiu I, Tapia-Otaegui G. Universal switched state-space representation for model predictive control of power converters. Electric Power Syst Res 2020;180:106120.

[3] Ma D, Chen W, Shu L, Qu X, Zhan X, Liu Z. A multiport power electronic transformer based on modular multilevel converter and mixed-frequency modulation. IEEE Trans Circ Syst II: Express Briefs. 2019. doi: 10.1109/TCSII.2019.2931529.

[4] Zhang G, Yuan J, Li Z, Yu SS, Chen S-Z, Trinh H, et al. Forming a reliable hybrid microgrid using electric spring coupled with non-sensitive loads and ess. IEEE Trans Smart Grid. 2020. doi: 10.1109/TSG.2020.2970486.

[5] Zhang G, Yuan J, Samson SY, Zhang N, Wang Y, Zhang Y. Advanced four-mode-modulation-based four-switch non-inverting buck–boost converter with extra operation zone. IET Power Electron. 2020. doi: 10.1049/iet-pel.2019.1540.

[6] Forouzesh M, Siwakoti YP, Gorji SA, Blaabjerg F, Lehman B. Step-up dc–dc converters: a comprehensive review of voltage-boosting techniques, topologies, and applications. IEEE Trans Power Electron 2017;32(12):9143–78.

[7] Peng FZ. Z-source inverters. Wiley Encyclopedia Electr Electron Eng 1999:1–11.

[8] Li D, Loh PC, Zhu M, Gao F, Blaabjerg F. Generalized multicell switched-inductor and switched-capacitor z-source inverters. IEEE Trans Power Electron 2012;28(2):837–48.

[9] Zhang G, Wang Z, lu HH-C, Chen S-Z, Ye Y, Zhang B, Zhang Y. Unique modular structure of multicell high-boost converters with reduced component currents. IEEE Trans Power Electron 2017;33(9):7795–804.

[10] Zhu B, Ding F, Vilathgamuwa DM. Coat circuits for dc–dc converters to improve voltage conversion ratio. IEEE Trans Power Electron 2019;35(4):3679–87.

[11] Zhao L, Chen J, Chen T, Shi Y, Fan Z, Zhuang Z. Zero-voltage and zero-current-switching dual-transformer-based full-bridge converter with current doubler rectifier. IEEE Trans Power Electron. 2020. doi: 10.1109/TPEL.2020.2997017.

[12] Dong S, Zhang Q. Ccm and dcm analysis of asc-qzsis. IET Power Electron 2019;12(8):2049–57.

[13] Lim SF, Khambadkone AM. A simple digital dcm control scheme for boost pfc operating in both ccm and dcm. IEEE Trans Ind Appl 2011;47(4):1802–12.

[14] De Gusseme K, Van de Sype DM, Van den Bossche AP, Melkebeek JA. Input-current distortion of ccm boost pfc converters operated in dcm. IEEE Trans Industr Electron 2007;54(2):858–65.

[15] Min R, Tong Q, Zhang Q, Zou X, Yu K, Liu Z. Digital sensorless current mode control based on charge balance principle and dual current error compensation for dc–dc converters in dcm. IEEE Trans Industr Electron 2015;63(1):155–66.

[16] Kim D-H, Choe G-Y, Lee B-K. Dcm analysis and inductance design method of interleaved boost converters. IEEE Trans Power Electron 2013;28 (10):4700–11.

[17] Hamill DC, Deane JH, Jefferies DJ. Modeling of chaotic dc-dc converters by iterated nonlinear mappings. IEEE Trans Power Electron 1992;7(1): 25–36.

[18] Chen Y, Chi KT, Qiu S-S, Lindenmuller L, Schwarz W. Coexisting fast-scale and slow-scale instability in current-mode controlled dc/dc converters: Analysis, simulation and experimental results. IEEE Trans Circ Syst I Regul Pap 2008;55 (10):3335–48.

[19] El Aroudi A, Rodríguez E, Leyva R, Alarcón E. A design-oriented combined approach for bifurcation prediction in switched-mode power converters. IEEE Trans Circ Syst II Express Briefs 2010;57(3):218–22.

[20] Hu T. A nonlinear-system approach to analysis and design of power-electronic converters with saturation and bilinear terms. IEEE Trans Power Electron 2010;26(2):399–410.

[21] Xiong X, Chi KT, Ruan X. Bifurcation analysis of standalone photovoltaic-battery hybrid power system. IEEE Trans Circ Syst I Regul Pap 2013;60 (5):1354–65.

[22] Shuai Z, Peng Y, Liu X, Li Z, Guerrero JM, Shen ZJ. Parameter stability region analysis of islanded microgrid based on bifurcation theory. IEEE Trans Smart Grid 2019;10(6):6580–91.

[23] Dai D, Tse C, Ma X. Symbolic analysis of switching systems: Application to bifurcation analysis of dc/dc switching converters. IEEE Trans Circ Syst I Regul Pap 2005;52(8):1632–43.

[24] Wan C, Huang M, Chi KT, Ruan X. Effects of interaction of power converters coupled via power grid: A design-oriented study. IEEE Trans Power Electron 2014;30(7):3589–600.

[25] Safaee A, Woronowicz K. Time-domain analysis of voltage-driven series–series compensated inductive power transfer topology. IEEE Trans Power Electron 2016;32(7):4981–5003.

[26] Li H, Guo Z, Liu C, Zheng TQ. An extensible stability analysis method in time domain for cascaded dc-dc converters in electrical vehicles. Microelectron Reliab 2018;88:1293–9.

[27] Scarciotti G, Astolfi A. Moment-based discontinuous phasor transform and its application to the steady-state analysis of inverters and wireless power transfer systems. IEEE Trans Power Electron 2016;31(12):8448–60.

[28] Zhang Z, Tian S, Ngo KD. Small-signal equivalent circuit model of quasi-square-wave flyback converter. IEEE Trans Power Electron 2017;32(8):5885–8.

[29] Bergna-Diaz G, Freytes J, Guillaud X, D'Arco S, Suul JA. Generalized voltage-based state-space modeling of modular multilevel converters with constant equilibrium in steady state. IEEE J Emerg Sel Top Power Electron 2018;6 (2):707–25.

[30] Ayachit A, Kazimierczuk MK. Averaged small-signal model of pwm dc-dc converters in ccm including switching power loss. IEEE Trans Circ Syst II Express Briefs 2018;66(2):262–6.

[31] Qu X, Jing Y, Lian J, Wong S-C, Chi KT. Design for continuous-current-mode operation of inductive-power-transfer converters with load-independent output. IET Power Electron 2019;12(10):2458–65.

[32] Zhang G, Zhang B, Li Z, Qiu D, Yang L, Halang WA. A 3-Z-network boost converter. IEEE Trans Ind Electron 2014;62(1):278–88.